Applied Catalysis B: Environmental 219 (2017) 501–510

Contents lists available at ScienceDirect

Applied Catalysis B: Environmental

journal homepage: www.elsevier.com/locate/apcatb

Research Paper

# Enhancing photoactivity for hydrogen generation by electron tunneling *via* flip-flop hopping over Möbius strip-like RGO

Zhen Li[a,b], Bin Tian[a,b], Wenlong Zhen[a,b], Wenyan Zhang[a], Xuqiang Zhang[a], Yuqi Wu[a], Gongxuan Lu[a,*]

[a] State Key Laboratory for Oxo Synthesis and Selective Oxidation Lanzhou Institute of Chemical Physics, Chinese Academy of Science, Lanzhou, 730000, China
[b] University of Chinese Academy of Science, Beijing, 100049, China

ARTICLE INFO

*Article history:*
Received 30 January 2017
Received in revised form 16 June 2017
Accepted 1 August 2017
Available online 2 August 2017

*Keywords:*
Möbius strip-like RGO
Rashba spin-orbit coupling
Flip-flop electron tunneling
Hydrogen evolution reaction

ABSTRACT

In this work, the Möbius strip-like reduced graphene oxide (RGO) was fabricated *via* $I_3^-$ and $I_5^-$ clusters, which offered a route for electron tunneling over RGO. This flip-flop electron tunneling took place *via* strong Rashba spin-orbit coupling between polyiodides and C atoms of RGO by the active electrons of polyiodides living in the p orbitals and it could bridge the easier charge transfer route between far-located carbon atoms at the edges of RGO through the polyiodides. This tunneling also restrained effectively the anisotropy of the electron transfer over RGO surface, achieving the rapid and efficient electron transfer over the surface of the RGO, resulting in remarkable increase of RGO conductivity and enhancing the lifetime of photogenerated charges. With the help of these properties, the obtained I-RGO/Ag photocatalyst presented a high $H_2$ generation activity under visible light irradiation. 318.8 μmol $H_2$ was evolved over I-RGO/Ag photocatalyst in 3 h, about 3.3 time higher than that of un-iodine RGO/Ag. In addition, no remarkable decay of $H_2$ evolution activity was observed in 1080 min reaction. The highest apparent quantum efficiencie (AQE) value of 28.8% was achieved at 430 nm.



## 1. Introduction

Möbius strips consist of end connected strip with twisting 180° angle, and have shown many potential applications in magnetic materials, sensors for small molecules and new classes of catalysts, etc [1–8]. For example, Zhao et al. [6] used a simple model of Möbius ladder to get higher energy band suppression of the transmission and the topology-induced optical spectral splitting. Ballon showed that Möbius topology played an important role in designing electronic instrumentation and novel materials. Nevertheless, even though researchers have been trying to synthesize different kinds of microscopic Möbius strip, only a few of such molecules have been achieved experimentally [5,9–11]. Two inorganic Möbius strips of $NbSe_2$ and $NbSe_3$ crystal based on the coordination chemistry of inorganic elements have been reported [9,10]. A twisted cyclic aromaticity with a Möbius topology has also been synthesized by design of the ligands and an appropriate choice of metal ions acting as connecting nodes. [5]

Recently, graphene has attracted extensive attention due to its remarkable structural and electronic properties [12–15]. A single graphene layer can be easily curved. Actually, graphene can be wrapped into carbon nanotube. This feature qualified graphene as a promising material to build Möbius strips. As a novel carbon nanostructure, graphene based Möbius strip was distinct from that of other carbon based low-dimension materials, such as carbon nanotube and graphene. In topology, the most outstanding feature of the graphene based Möbius strip is that it has only one edge and one surface [16–18]. Besides, graphene based Möbius strip is a stable structure and shows novel optical and magnetic properties. Especially, it might resolve the anisotropy of electron transfer on the surface of graphene, which seriously impede the application of graphene.

For photocatalytic hydrogen evolution reaction, charge-pair formation, transfer and reaction are known as a key point to obtain high efficientcy [19–22]. Graphene material is believed to enhance the electron transfer rate effectively and to reduce the carrier recombination [23,24]. Graphene is built by adjacent carbon atoms *via* both σ bond and π bond. Although the electron of the σ bond is strongly restricted by the atom core, the π bond is relatively delocalized. The π bonds can create π ribbons to provide a tunneling route for the electron transfer, [25] leading to better

* Corresponding author at: State Key Laboratory for Oxo Synthesis and Selective Oxidation Lanzhou Institute of Chemical Physics, Chinese Academy of Science, Lanzhou, 730000, China.
*E-mail address:* gxlu@lzb.ac.cn (G. Lu).

http://dx.doi.org/10.1016/j.apcatb.2017.08.003
0926-3373/

conductivity for high effective photocatalytic $H_2$ evolution [26]. However, graphene materials are usually hard to produce ideal crystals because of the effect of residual oxygen functional groups and vacancy defects [27,28]. These defects can affect their electrical conductivity significantly. In addition, the electron transfer between two sides of graphene is also inhibited. Searching a special channel is the key point for electron rapid transfer on the surface and between two sides of graphene to reduce the photogenerated charges recombination.

In general, the electrical conductivity of the graphene material could be changed and promoted by doping the heteroatoms with different electronic characteristics into the graphene framework. And it was widely studied in designing and fabricating the tunable device based on graphene [29–32]. For example, Yao et al. found that the iodine doped graphene showed an advantageous charge distribution and effective oxygen reduction reaction activity. [32] Kalita et al. proved that the iodinated graphene had superior electrochemical performance due to the change of graphene lattice and defects [33]. In addition, many efforts had also been done to improve the electrical conductivity of the graphene materials by doping iodine species in fuel cells [34]. For example, Zhan et al. reported the iodinated graphene showed higher reversible capacity, longer-term cyclability and more excellent rate performance with very high current density, leading to effective electrochemical activity [35]. The $I_3^-$ and $I_5^-$ interacted with carbon atoms by an electron transfer process could reduce the resistance of carbon materials and improve the electron transfer [36,37]. More than that, our recent work suggested that the exceptional electrical properties of $I_3^-$ and $I_5^-$ clusters decorated graphene might attribute to a larger Rashba spin-orbit coupling induced by heavy atoms with active electrons living in p orbitals [38–40]. The tunneling opened by the polyiodides p orbitals could lead an electron hopping between two far-located carbon atoms of g-$C_3N_4$ and RGO, which give the superior charge transfer performance. In addition, graphene edges could provide decent adsorption sites for halogen atom combination, that was also proved by first-principle density-functional calculations [41]. Therefore, we deduce that the polyiodides could open tunneling at the edges of RGO for constructing Möbius strip-like graphene to enhance the electron transfer.

In this paper, we developed a route for fabrication of Möbius strip-like RGO photocatalyst by *in situ* AgI nanoparticles (NPs) decomposition using light irradiation method. The formed polyiodides opened an electron tunneling at the edges of RGO by strong Rashba spin-orbit coupling. The flip-flop electron tunneling bridged the easier transfer route between far-located carbon atoms at the edges of RGO through the polyiodides p orbitals for constructing the Möbius strip-like RGO to restrain effectively the anisotropy of the electron and enhance the electron transfer on the surface of RGO. The structure and chemical states of iodine species were characterized through XPS and XRD spectroscopy.

## 2. Experimental section

### 2.1. Materials

Graphite powder (<33 μm, CP, Sinopharm Chemical Reagent Co., Ltd.), $H_2SO_4$ (98%, AR, Baiyin Liangyou Reagent Co., Ltd), $P_2O_5$ (AR, Chengdu Kelong Chemical Reagent Factory), $K_2S_2O_8$ (AR, Sichuan Xilong Chemical Industry Co., Ltd.), $NaNO_3$ (AR, J&K Scientific Ltd.), $KMnO_4$ (AR, J&K Scientific Ltd.), $H_2O_2$ (30%, AR, Tianjin Hongyan Chemical Reagent Factory), HCl (37%, AR, Baiyin Liangyou Reagent Co., Ltd.), $BaCl_2$ (AR, Sinopharm Group Chemical Reagent Co., Ltd.), $NaBH_4$ (AR, Sinopharm Group Chemical Reagent Co., Ltd.), $AgNO_3$ (AR, J&K Scientific Ltd.), KI (AR, J&K Scientific Ltd.), NaOH (AR, Sinopharm Group Chemical Reagent Co., Ltd.), EY (AR, Sinopharm Group Chemical Reagent Co., Ltd.), TEOA (AR, Sinopharm Group Chemical Reagent Co., Ltd.), all the reagents were used without any further purification.

### 2.2. Preparation of the RGO photocatalyst

Graphene oxide (GO) was prepared from natural graphite by using a modified Hummers method [42,43]. Typically, graphite powder (100 g) was added to an 80 °C mixture solution of concentrated $H_2SO_4$ (150 mL), $P_2O_5$ (50 g), and $K_2S_2O_8$ (50 g). The resultant mixture was isolated and allowed to cool down to room temperature. Then the mixture was diluted with distilled water (7.5 L) and the product was filtered, washed with distilled water until the filtrate pH become neutral. The product was dried in air at room temperature for 24 h. Subsequently, the preoxidized graphite (20 g) and $NaNO_3$ (10 g) were added to cold concentrated $H_2SO_4$ (0 °C, 460 mL). $KMnO_4$ (60 g) was then added gradually with stirring and cooling so that the temperature of the mixture was kept below 20 °C. The mixture was then stirred at 35 °Cfor 2 h. Distilled water (920 mL) was slowly added to the mixture, followed by stirring for 15 min. The reaction was terminated by adding distilled water (2.8 L) and then $H_2O_2$ solution (50 mL, 30%). The product was filtered, washed repeatedly with HCl (1:10, v/v) until sulfate could not be detected with $BaCl_2$, and then dried in a vacuum oven at 40 °Cfor 24 h.

Aqueous dispersions of RGO (2 mg $mL^{-1}$) were prepared by reducing GO with sodium borohydride ($NaBH_4$) as a reductant. In a typical synthetic procedure, 500 mg of graphene oxide powder was dispersed into 250 mL of distilled water with the ultrasound treatment (25 kHz, 250 W) until the solution become clear. The obtained yellow-brown dispersions of graphene oxide were then heated to 95 °C in an oil bath under magnetic stirring. After stirring for few minutes, 2 g of $NaBH_4$ was added to the aqueous dispersions, and the reduction reaction was maintained at this temperature for 10 h, over which the color of the solution gradually changed into dark black, indicating the reduction of GO. After the reaction, the obtained dispersions was filtered, washed with water several times, and finally redispersed in water with ultrasonic treatment prior to use.

### 2.3. Photocatalytic $H_2$ evolution activity and AQE measurements

Photocatalytic experiments were performed in a sealed Pyrex flask (150 mL) with a flat window (an efficient irradiation area of 14 $cm^2$) and a silicone rubber septum for sampling at ambient temperature. In a typical reaction system, 2 mL 2 mg/mL RGO aqueous dispersion was added into 100 mL 10% (v/v) triethanolamine (TEOA) aqueous solution. After 30 min ultrasonic treatment, 0.1 mL 20 mg/mL $AgNO_3$ aqueous solution was added into the suspension drop by drop and then the stoichiometric KI aqueous solution was added in the same way. This dispersion was stirred for 30 min and 70 mg eosin Y (EY) was added into. Prior to irradiation, the suspension mixture was degassed by bubbling Ar gas for 30 min. The light source was a 300-W Xe lamp (NBeT Technology Co., Ltd), which equipped with either a 420 nm cut-off filter or various band-pass filters. Photon flux of the incident light was determined using a Ray virtual radiation actinometer (FU 100, silicon ray detector, light spectrum, 400–700 nm; sensitivity, 10–50 μV $\mu mol^{-1} m^{-2} s^{-1}$). The amount of $H_2$ was measured using gas chromatography (Agilent 6820, TCD, 13 × column, Ar carrier), and the AQE was calculated from the equation below:

$$\text{AQE} = 2 \times \text{number of evolved } H_2\text{molecules} / \text{number of incident photos} \times 100\%$$

### 2.4. Isotopes tracer experiment

The isotopes tracer experiments have been performed in a sealed Pyrex reactor. A certain amount of RGO and TEOA was added in 10 mL $D_2O$. After 30 min ultrasonic treatment, stoichiometric $AgNO_3$ and KI power were added in the suspension in sequence under the condition of stirring. This dispersion was stirred for 10 min and 70 mg EY was added into. Prior to irradiation, the suspension mixture was degassed by bubbling Ar gas for another 30 min. The light source was a 300-W Xe lamp, which equipped with either a 420 nm cut-off filter. The $D_2$ was measured by GC–MS (MAT 271).

### 2.5. Working electrode preparation and photoelectrochemical measurements

Photocurrent responses of catalyst samples were measured on an electrochemical analyzer (CHI660E) in a homemade standard three-compartment cell, consisting of an organic glass enclosure with a quartz window and a 1.2 cm diameter opening opposite the window to the work electrode was clamped. The working electrodes were prepared by drop-coating sample suspensions directly onto the precleaned indium tin oxide glass (ITO glass) surface by microsyringe with an infrared heat lamp to speed drying. The surface of working electrode exposed to the electrolyte was a circular film with the geometrical surface areas of 1 $cm^2$. Platinum foil was used as a counter electrode and a saturated calomel electrode (SCE) was used as the reference electrode. The supporting electrolyte was 10% TEOA aqueous solution mixed with 0.1 M $Na_2SO_4$ aqueous solution. A 300-W Xe lamp with an optical cutoff filter ($\lambda \geq 420$ nm) was used for excitation light source. The unbiased anodic photocurrent was investigated with an amperometric current-time technique.

### 2.6. Characterizations

Transmission electron microscopy (TEM) images were taken with a Tecnai-G2-F30 field emission transmission electron microscope operating at accelerating voltage of 300 kV. The X-ray diffraction patterns (XRD) of the samples were recorded on a Rigaku B/Max-RB X-ray diffractometer with a nickel-filtrated Cu Kα radiation. The accelerating voltage and current were 40 kV and 30 mA, respectively. XPS analysis was performed using a VG ScientificESCALAB210-XPS photoelectron spectrometer with a Mg KRX-ray resource. The fluorescence decay times and PL spectra were measured using the Horiba Jobin Yvon Data Station HUB operating in time-correlated single photon counting mode (TCSPC) with the time resolution of 200 ps. Nano LED diode emitting pulse sat 460 nm with 1 MHz repetition rate was used as an excitation source. Light-scattering Ludox solution was used to obtain the instrument response function (prompt). The time ranges are0.055 ns/channel in 4096 effective channels. Horiba Jobin Yvon DAS6 fluorescence decay analysis software was used to fit the model functions to the experimental data. The I–V curves of the specimens were measured by the 2-probe method on a Keithley 4200 semiconductor characterization system (electrode contact area of $2.56 \times 10^{-6}$ $m^2$) at room temperature in air environment.

## 3. Results and discussion

The Scheme 1 shows the forming process of the Möbius strip-like RGO constructed by polyiodides. The calculated amount of RGO aqueous dispersion was added into 100 mL 10% (v/v) TEOA solution and subsequently dispersed by ultrasound to achieve homogeneous RGO dispersion. After that, the calculated amount $AgNO_3$ aqueous solution was also added into the suspension drop by drop

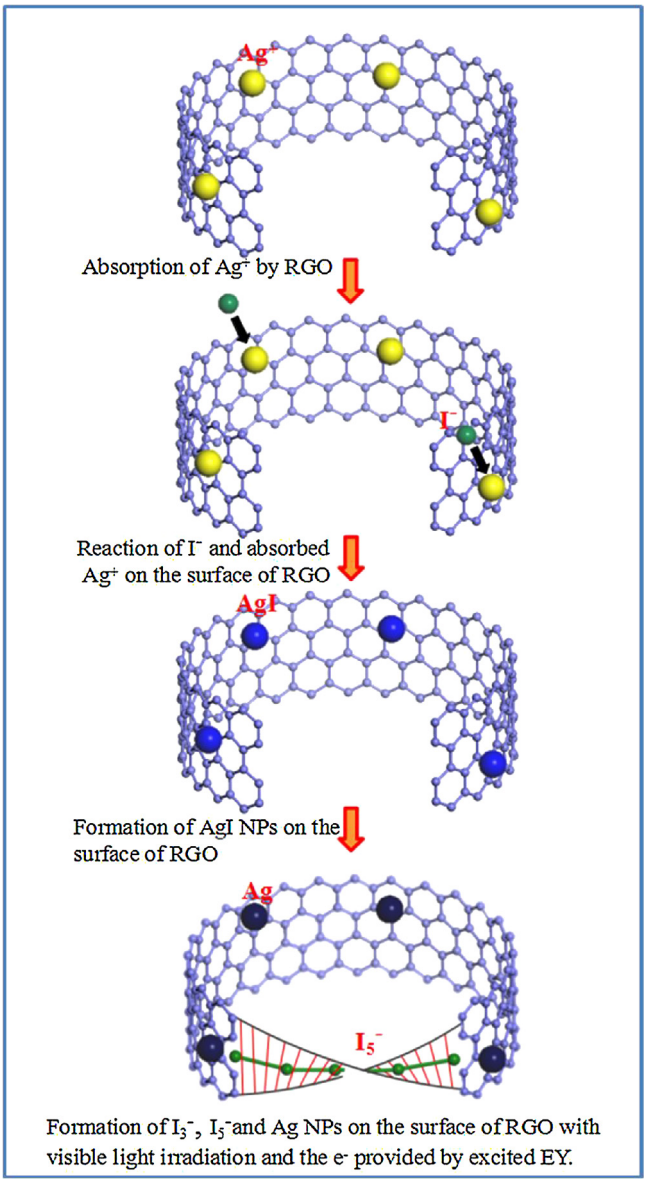


**Scheme 1.** The forming process of the Möbius strip-like RGO constructed by polyiodides.

under stirring condition, in this process, the $Ag^+$ ions were primarily adsorbed on the surface of RGO by coulomb forces due to the negative charge of RGO. After stirring ten minutes, the stoichiometric KI aqueous solution was added in the same way to achieve AgI/RGO composite. With the help of electron provided by excited EY and the visible light irradiation, the AgI NPs were decomposed to further form Ag NPs and polyiodides. The polyiodides could bridge the far-located carbon atoms at the edges of RGO to construct Möbius strip-like RGO. In order to prove the formation of Ag NPs and polyiodides decomposed by the AgI NPs, the XRD characterization of RGO, I-RGO, RGO/Ag and I-RGO/Ag photocatalysts were performed as shown in Fig. 1. The strongest diffraction peak of the RGO photocatalyst at 24.2° was assigned to the (002) facet of RGO. The peak centered at 10.6° was assigned to (001) facet of RGO. After loading Ag or AgI NPs on the surface of RGO, a series of new peaks centered at 38.1, 44.2, 64.5, 77.5, 81.3° were detected, which could be attributed to (111), (200), (220), (311) and (222) facets of metal Ag, respectively. This result suggests that the AgI NPs was decomposed to form Ag NPs on the surface of RGO. However, the diffraction peaks of RGO was weaken obviously after loading Ag or AgI specie

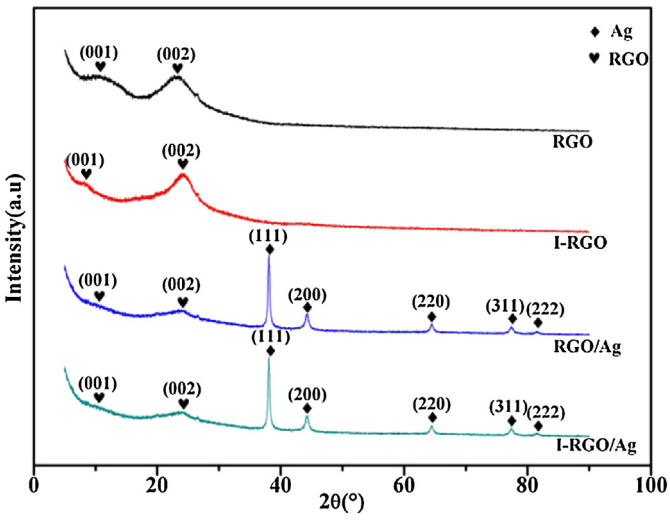


**Fig. 1.** Experimental XRD patterns for RGO, I-RGO, RGO/Ag and I-RGO/Ag photocatalysts.

on the surface of RGO, indicating that a strong interaction existed between the Ag NPs and RGO. In addition, there were no obvious changes on the diffraction peaks of RGO and no other peaks were detected when $I^-$ was added in the RGO dispersion.

The XPS spectra of RGO, I-RGO, RGO/Ag and I-RGO/Ag photocatalysts were performed to study the chemical states of Ag and I species as shown in Fig. 2. In Fig. 2A, there was no obvious shift of binding energy peaks for the different photocatalysts and four kinds of chemical states of C atoms in the RGO was detected. As shown in the insert of Fig. 2A, the strongest peak centered at 284.8 eV could be assigned to $sp^2$-bonded carbon (C—C) species, while the weaker one centered at 286.3 eV could be assigned to $sp^3$-bonded carbon (C—OH) species. The peak at 288.2 eV was assigned to $sp^3$-bonded carbon (C—O-C) species and the weakest one at 289.3 eV was assigned to $sp^2$-bonded carbon (O=C—O) species [44–46]. In Fig. 2B, the binding energy of the Ag species showed that Ag was in the metal state and a slight difference between the RGO/Ag and I-RGO/Ag photocatalysts was detected. This result might be caused by the effect of I species. In Fig. 2C, the peaks centered at 618.3 and 619.6 eV were attributed to $I_3^-$ and $I_5^-$ $3d_{5/2}$ and the peaks centered at 630.0 and 631.9 eV were attributed to $I_3^-$ and $I_5^-$ $3d_{3/2}$, suggesting I species existed in the form of $I_3^-$ and $I_5^-$ clusters in the I-RGO/Ag photocatalyst. This result suggested that the polyiodides could open an electron tunneling at the edges of RGO [38–41]. The flip-flop electron tunneling takes place *via* strong Rashba spin-orbit coupling between polyiodides and C atoms of RGO for constructing Möbius strip-like RGO by polyiodides active electrons living in the p orbitals. However, for the I-RGO photocatalyst, the peaks centered at 620.8 and 632.3 eV was detected, which implied the I specie existed in the form of $I^-$ ion in I-RGO photocatalyst.

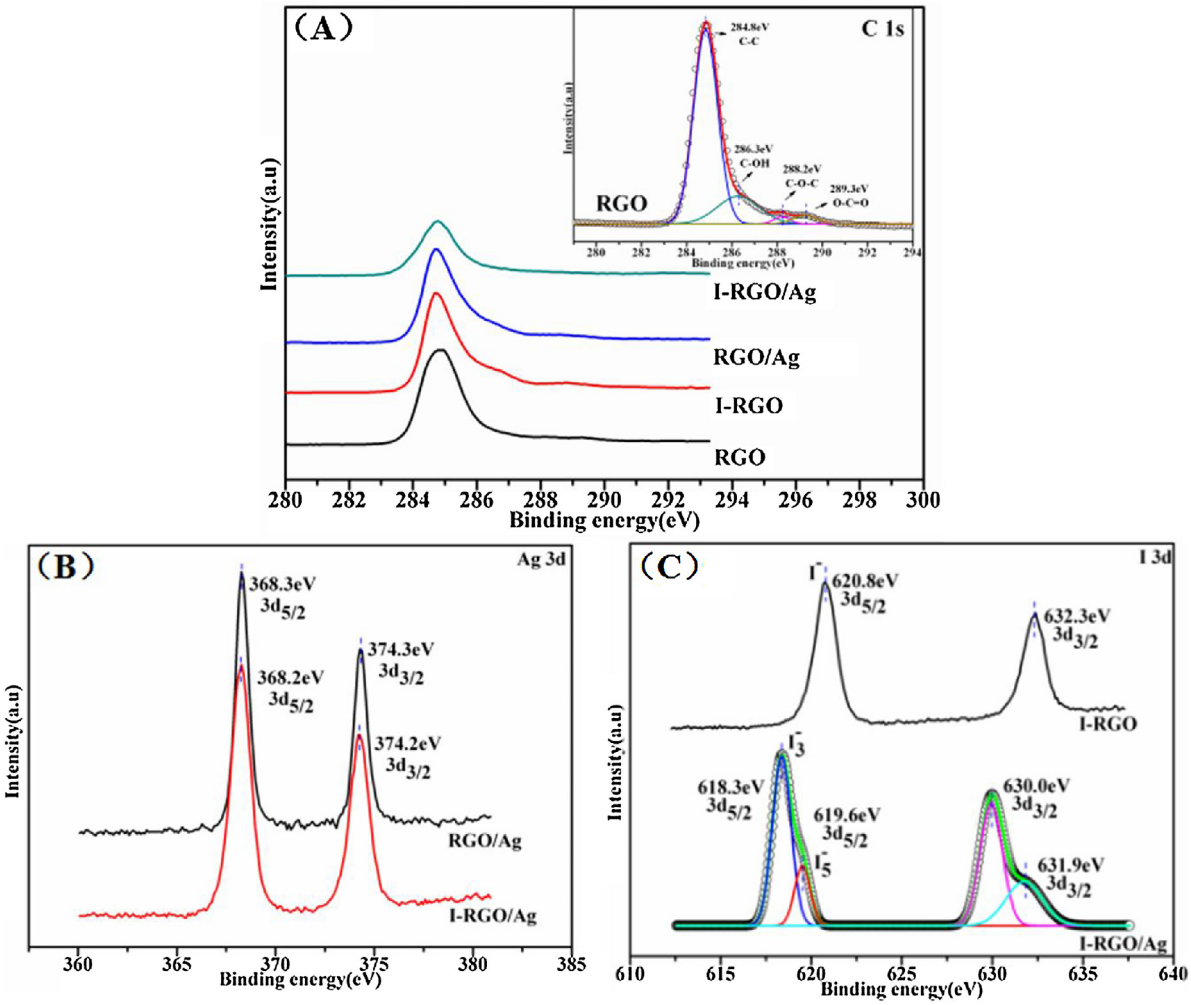


**Fig. 2.** The XPS spectra of RGO, I-RGO, RGO/Ag and I-RGO/Ag photocatalysts. A) C1 s specta. B) Ag 3d spectrum. C) I 3d spectrum.

**Table 1**
Fluorescence lifetime measurements of EY in RGO, I-RGO, RGO/Ag and I-RGO/Ag dispersion.

| RGO systems | Lifetime, <τ> (ns) | Pre-exponential factors *B* | Average lifetime,<τ> (ns) | $\chi^2$ |
|---|---|---|---|---|
| EY | $\tau_1$ = 1.25 | $B_1$ = 1 | 1.25 | 1.0032 |
| EY-RGO | $\tau_1$ = 1.27 | $B_1$ = 0.8031 | 1.37 | 1.0061 |
| | $\tau_2$ = 1.78 | $B_2$ = 0.1969 | | |
| EY-I-RGO | $\tau_1$ = 1.27 | $B_1$ = 0.8014 | 1.38 | 0.9974 |
| | $\tau_2$ = 1.81 | $B_2$ = 0.1986 | | |
| EY-RGO/Ag | $\tau_1$ = 1.73 | $B_1$ = 0.5727 | 2.34 | 1.0009 |
| | $\tau_2$ = 3.15 | $B_2$ = 0.4273 | | |
| EY-I-RGO/Ag | $\tau_1$ = 1.69 | $B_1$ = 0.4872 | 2.68 | 1.0018 |
| | $\tau_2$ = 3.63 | $B_2$ = 0.5128 | | |

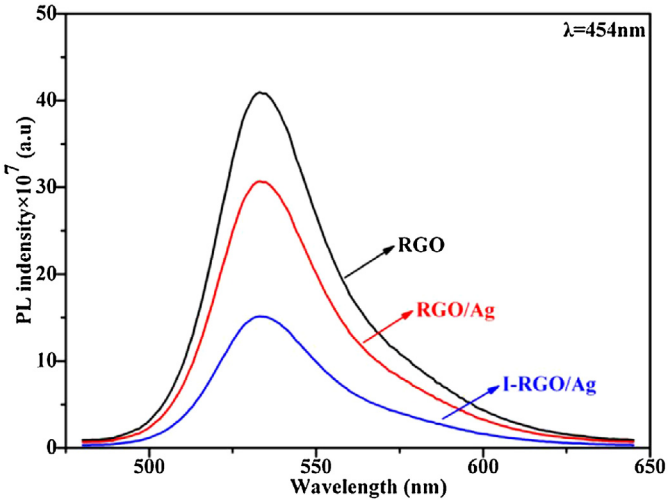


**Fig. 3.** PL spectra of EY in RGO, RGO/Ag and I-RGO/Ag dispersion.

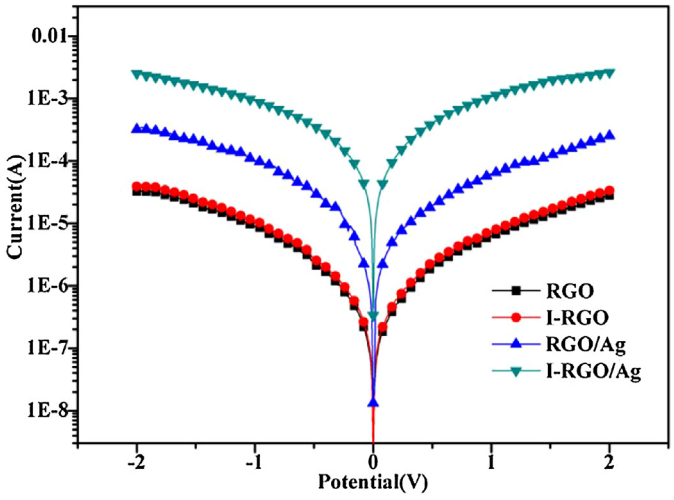


**Fig. 4.** The I–V electrochemical curve of RGO, I-RGO, RGO/Ag and I-RGO/Ag photocatalysts. (1/R = I/U).

The PL spectra were measured to prove the electron transfer rate on the surface of RGO could be promoted by polyiodides and the result was shown in Fig. 3. The strongest PL of EY in RGO dispersion indicated the fast photogenerated carrier recombination. However, after loading Ag NPs on the surface of RGO, an obvious quenching effect has been detected, which suggested that a strong interaction existed between RGO and Ag NPs, this interaction could enhance the electron transfer rate from EY to RGO and subsequently from RGO to Ag NPs, resulting in the reduce of the photogenerated carriers recombination. In addition, the quenching effect was further enhanced after the Möbius strip-like RGO constructed by the polyiodides, this resulted indicated the Möbius strip-like RGO could promote the electron transfer rate, which could further enhance carriers separation and prolong of photogenerated electron lifetime to achieve highly efficient $H_2$ generation activity. The data of fluorescence lifetime came to a same conclusion as shown in Table 1. The emission decay of EY solution was single-exponential in TEOA aqueous, suggesting that there was only one emitting species (monomeric EY molecules). After addition of RGO into TEOA aqueous solution, the emission decay was two-exponential [47]. The long-lived (1.78 ns) and short-lived (1.27 ns) species were probably due to the EY molecules interacted with RGO and the monomeric EY molecules [48]. This result implied that there was an interaction between RGO and EY and the electron could fast transfer from excited EY on the surface of RGO [49]. However, loading $I^-$ ion on the surface of RGO, the lifetime didn't change obviously, implying that the $I^-$ ion was no contribution to prolong the electrons lifetime. Loading Ag NPs on the surface of RGO, the average lifetime was increased from 1.37 ns to 2.34 ns, which also suggested an interaction existed between RGO and Ag NPs. In this process, the interaction could enhance the electron transfer from RGO to Ag NPs. In addition, after Möbius strip-like RGO formed, the average lifetime was further prolonged (2.68 ns), which further confirmed the Möbius strip-like RGO could promote the electron transfer rate on the surface RGO and remarkably prolong the lifetime of photogenerated electron to reduce the recombination of carriers [12,50]. The I–V electrochemical curve was performed to further study the effect of polyiodides on the electron transfer rate as shown in Fig. 4. In Fig. 4, the series photocatalysts all exhibited typical conductor property. However, loading Ag NPs on the surface of RGO, the current for the RGO was greatly increased by one order of magnitude compared to that of the pristine RGO. This result showed that the Ag NPs could improve the electrical conductivity of RGO to promote the electron transfer rate. In addition, the electrical conductivity of RGO/Ag photocatalyst was further enhanced by two orders of magnitude compared to that of the pristine RGO with forming Möbius strip-like RGO, implying that the polyiodides could also greatly improve the electrical conductivity of RGO. It was a good agreement with the result of fluorescence lifetime.

TEM was carried out to study the structure and morphology of I-RGO, RGO/Ag and I-RGO/Ag photocatalysts and the results were shown in Fig. 5. In Fig. 5A and 5C, the Ag specie was distributed uniformly on the surface of RGO in the form of NPs and the edge of RGO appeared a large amount of folding part. These fold structures will provide the sites for polyiodides loading on to construct the Möbius strip-like RGO. The HRTEM image of RGO/Ag and I-RGO/Ag photocatalysts showed that the Ag species were well crystalized. The lattice spacing of 0.23 nm could be assigned to (111) facet of metal Ag. This result further proved that the Ag specie was in the form of metal Ag on the surface of RGO. In Fig. 5E, the element composition clearly showed that the distribution of C, O, and I elements

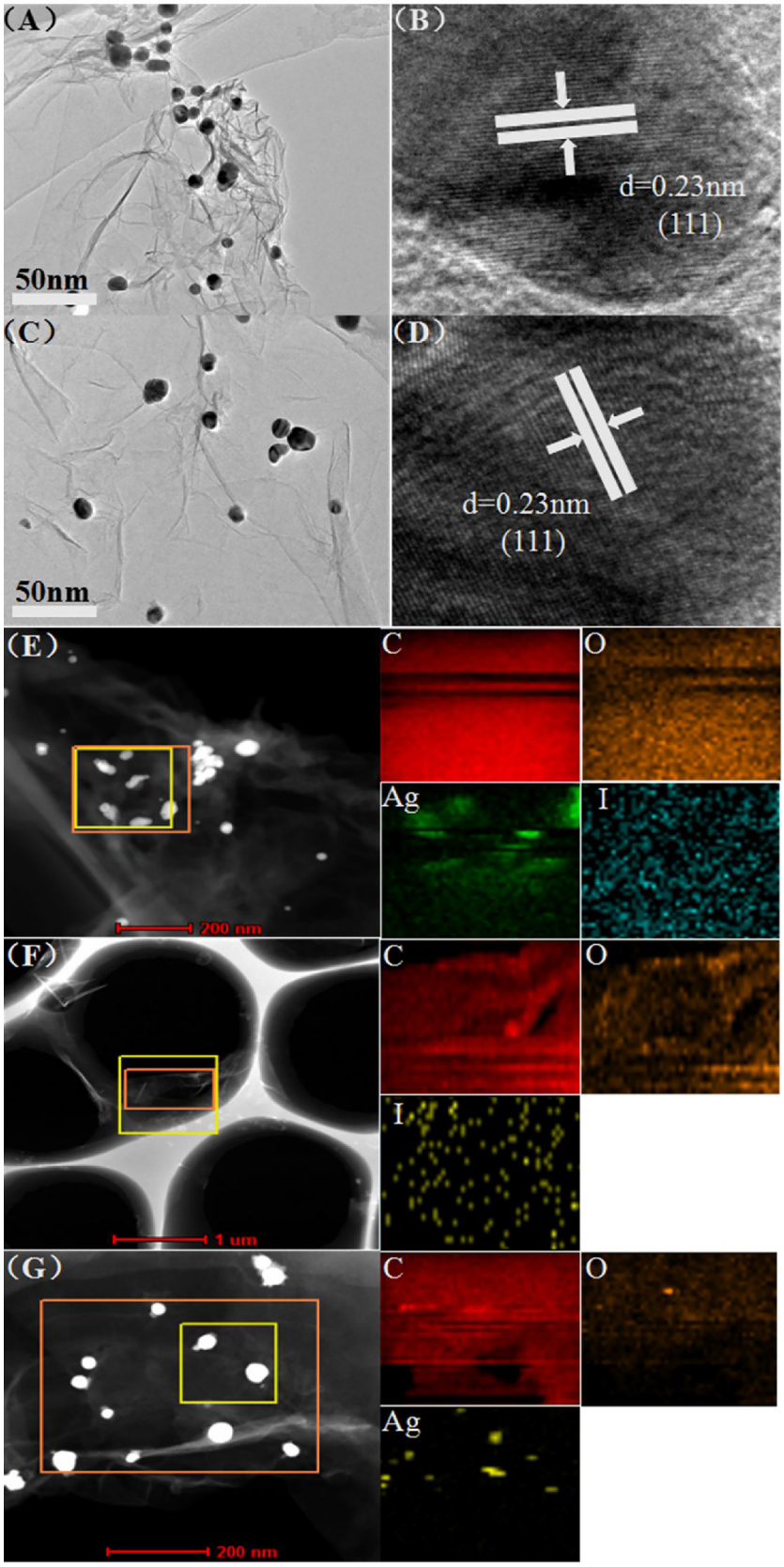


**Fig. 5.** Transmission electron microscopy images of I-RGO/Ag (A) and RGO/Ag photocatalyst (C); The high-resolution transmission electron microscopy image of I-RGO/Ag (B) and RGO/Ag photocatalyst (D); elemental mapping images of I-RGO/Ag (E), RGO/Ag (F) and I-RGO (G) photocatalysts.

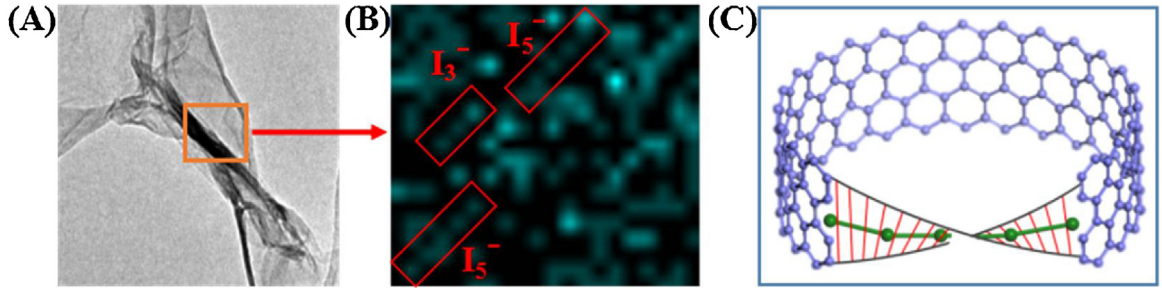


**Fig. 6.** TEM image of I-RGO/Ag photocatalyst (A); the elemental mapping image of I-RGO/Ag photocatalysts (B) and the model of Möbius strip-like RGO (C).

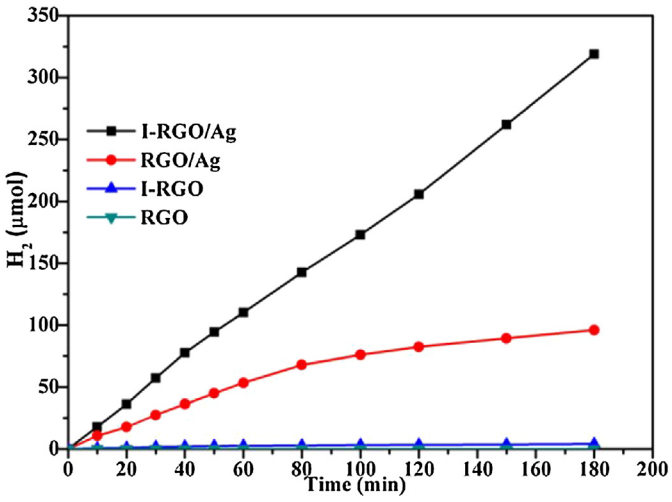


**Fig. 7.** The time courses of $H_2$ evolution catalyzed by I-RGO/Ag, RGO/Ag, I-RGO and RGO with EY sensitization in 10% (v/v) TEOA aqueous solution under visible light irradiation (λ≥420 nm) conditions at pH 11.

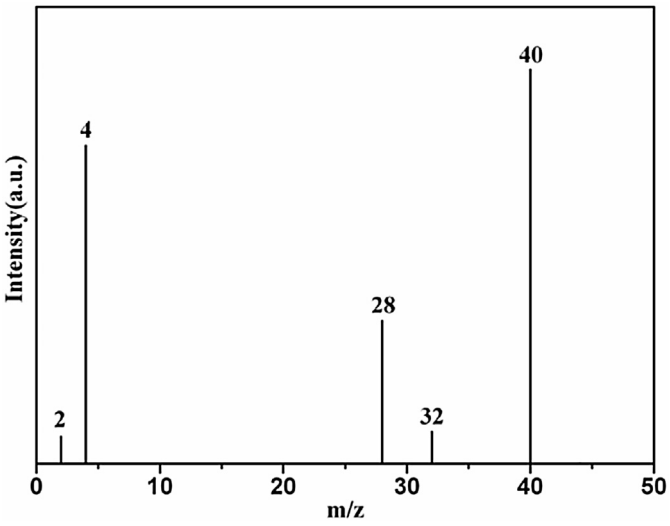


**Fig. 8.** GC–MS spectra obtained after injecting 0.5 mL samples of the gas phase species produced by $D_2O$ splitting over I-RGO/Ag photocatalyst in a sealed Pyrex flask under visible light irradiation for 2 h.

were relatively homogeneous in I-RGO/Ag photocatalyst and the I specie was in the form of chain. In addition, the metal Ag was in the form of NPs. The same conclusion was also achieved by the element composition of RGO/Ag photocatalyst as shown in Fig. 5F. In Fig. 5G, the $I^-$ ion were uniformly distributed on the surface of RGO, but the amount of $I^-$ ion was trace. The Fig. 6 showed the typical Möbius strip-like RGO constructed by the polyiodides *via* connecting the folding part of RGO. The Fig. 6B suggested a large amount of the polyiodides existed in the folding part of RGO selected in the square field in Fig. 6A. This resulted further proved the Möbius strip-like RGO constructed successfully by the polyiodides. And the model of Möbius strip-like RGO was showed in Fig. 6C.

The time courses of $H_2$ evolution in 10% (v/v) TEOA aqueous solution under visible light irradiation (λ≥420 nm) conditions were performed over I-RGO/Ag, RGO/Ag, I-RGO and RGO photocatalysts as shown in Fig. 7. No $H_2$ was detected over RGO photocatalyst and only a trace amount of $H_2$ generated over I-RGO photocatalyst. This result suggested the RGO and I-RGO photocatalysts were inactivity for $H_2$ evolution. However, after loading Ag NPs on the surface of RGO, 96.1 μmol was evolved in 3 h, which indicated the Ag NPs as a co-catalyst could provide an active site for $H_2$ evolution. In addition, with the Möbius strip-like RGO formed, the $H_2$ generation activity was further improved greatly about 318.8 μmol in 3 h. This result further confirmed that the Möbius strip-like RGO polyiodides could restrain effectively the anisotropy of the electron and promote the electron transfer rate by polyiodides opening an electron tunneling at the edges of RGO, leading to efficient $H_2$ evolution activity [38–40]. In order to prove the $H_2$ generated from water, the isotopic tracer experiment was carried out and the result was shown in Fig. 8. The isotopes analysis results showed both $D_2$ and $H_2$ were

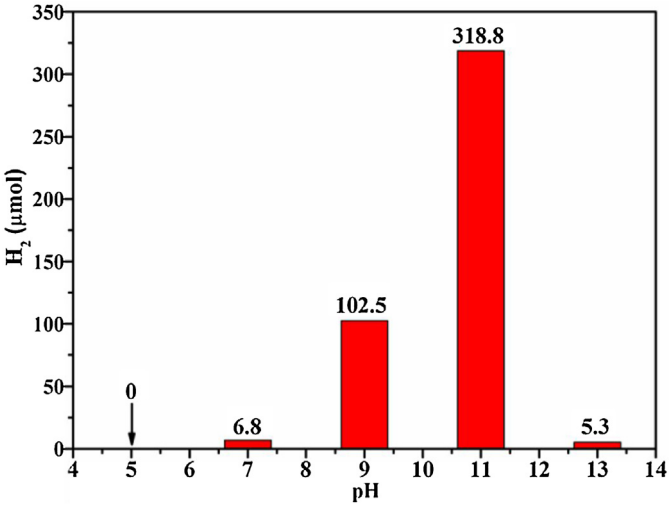


**Fig. 9.** The effect of pH on photocatalytic activity of I-RGO/Ag photocatalyst with EY sensitization for hydrogen evolution.

detected. It indicated the $D_2$ comes from water splitting. The m/z signal at 28, 32 and 40 correspond to the $N_2$, $O_2$ and Ar gas [51].

The activities of $H_2$ evolution at different pH (5, 7, 9, 11 and 13) were investigated to optimize the reaction condition as shown in Fig. 9. At pH 11, $H_2$ evolution could be achieved the highest activity. It was about 318.8 μmol $H_2$ evolved over I-RGO/Ag photocatalyst in EY sensitized suspension dispersion. With the acidity

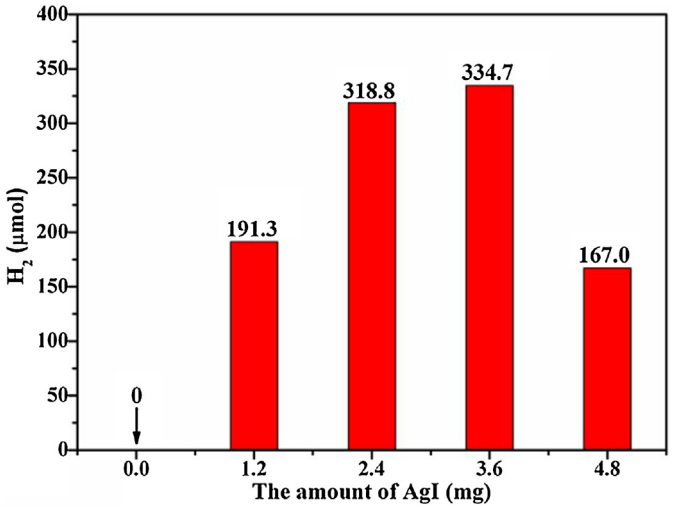


**Fig. 10.** The effect of the amount of AgI on the activity of $H_2$ evolution over 4 mg RGO photocatalyst under visible light irradiation (λ≥420 nm).

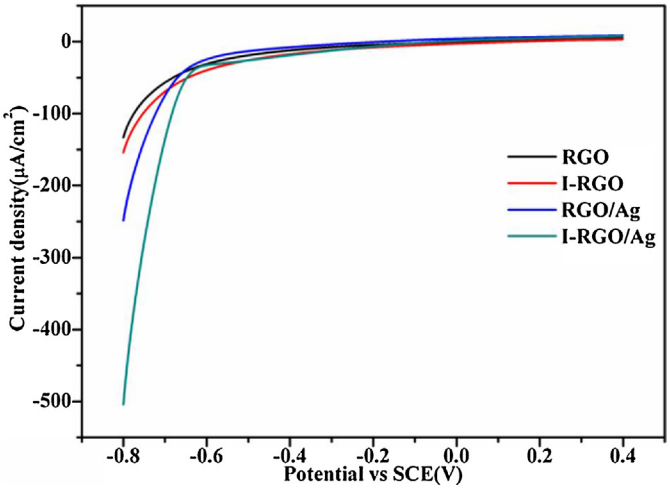


**Fig. 12.** LSV curves of I-RGO/Ag, RGO/Ag, I-RGO and RGO photocatalysts coated on ITO glass in mixed solution of 10% (v/v) TEOA and 0.1 M $Na_2SO_4$ aqueous solution.

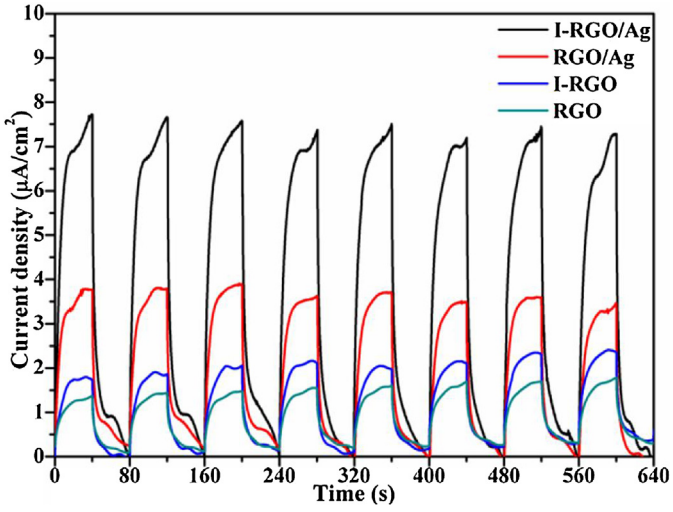


**Fig. 11.** Transient photocurrent time profiles of I-RGO/Ag, RGO/Ag, I-RGO and RGO photocatalysts with EY sensitization on ITO glass in mixed solution of 10% (v/v) TEOA and 0.1 M $Na_2SO_4$ at pH 11 under visible light irradiation (≥420 nm).

increased, the $H_2$ evolution activity gradually decreased resulted by the protonation of TEOA in acidic solution [47]. The process of protonation would impact the electron-donating properties of TEOA and the absorption performance of EY in the visible light region. On the other hand, with the alkaline increased,the $H_2$ evolution activity was also gradually decreased and only 5.3 μmol of $H_2$ was detected in 3 h at pH 13. It resulted from the decrease of proton concentration and the fact that $H_2$ evolution became more thermodynamically unfavorable with increasing pH values [51–60]. The effect of the amount of AgI loading on the surface of RGO was also performed to optimize the reaction condition and the results were shown in Fig. 10. The activity of $H_2$ evolution increased with the AgI increased. When the amount of AgI was 3.6 mg, it could achieve the highest $H_2$ evolution activity, corresponding to 318.8 μmol in 3 h. Further increase of the amount of AgI, the activity of $H_2$ evolution was decreased. This result might result from the Ag NPs agglomeration, which led to exposed less active site for $H_2$ evolution reaction [39].

Photoelectrochemical experiments were performed to study the photoinduced electron transfer processes and the result was shown in Fig. 11. As we can see, the RGO/ITO and I-RGO/ITO electrodes produced a low photocurrent. However, after loading Ag NPs on the surface of RGO, the observed unbiased transient photocurrent was promoted under similar experimental conditions. The maximum photocurrent of 3.9 μA/cm$^2$ was achieved after sensitized by EY. This result implied that the Ag NPs could enhance the photogenerated electron transfer rate from excited EY to RGO. In addition, with the formation of Möbius strip-like RGO, the photocurrent was further enhanced, resulting in the maximum photocurrent of 7.8 μA/cm$^2$. It also confirmed that the Möbius strip-like RGO could enhance the electron transfer on the surface of RGO, which remarkably reduced the recombination of carrier and prolonged the lifetime of photogenerated electron, leading to excellent photocurrent [60–66]. The electrochemical $H_2$ evolution activities of I-RGO/Ag, RGO/Ag, I-RGO and RGO photocatalysts deposited on ITO glass were also investigated using the LSV technique. As shown in Fig. 12, the RGO/ITO and I-RGO/ITO electrodes exhibited low cathodic currents. However, the RGO/Ag/ITO electrode achieved the significant improved cathodic currents at −0.6 V, which further proved that Ag NPs were active sites for $H_2$ evolution. Moreover, after the Möbius strip-like RGO formed, the photocurrent density was further enhanced, about 500 μA/cm$^{-1}$ was achieved at −0.6 V. It further confirmed that the polyiodides could promote the electron transfer rate on the surface of RGO to remarkably reduce the recombination of carrier and prolonged the lifetime of photogenerated charges.

The apparent quantum efficiencies (AQEs) were investigated in the range of 430 ~ 550 nm using various bandpass filters (λ= 430, 460, 490, 520, and 550 nm) as shown in Fig. 13. The highest AQE value of 28.8% was achieved at 430 nm. With the incident light wavelength increased, the AQEs value decreased gradually due to the lower power of photons [61]. However, the AQE value was relative high at 520 nm because of the highest absorption of EY at 518 nm. This result also indicated that the EY had an interaction with RGO, which could lead the electron to transfer faster from excited EY to RGO. The stability of $H_2$ evolution over I-RGO/Ag photocatalyst sensitized by EY were carried out under visible light irradiation (λ ≥ 420 nm). As shown in Fig. 14, no obvious change for $H_2$ evolution rate was detected during 1080 min reaction, this result suggested the I-RGO/Ag photocatalyst exhibited excellent stability.

The reaction mechanism of photocatalytic $H_2$ evolution over I-RGO/Ag photocatalyst was illustrated in the Scheme 2. The EY molecule absorbed the photon to form singlet excited state $EY^{1*}$ under visible light irradiation, subsequently, produced the lowest-lying triplet excited state $EY^{3*}$ *via* an efficient intersystem crossing.

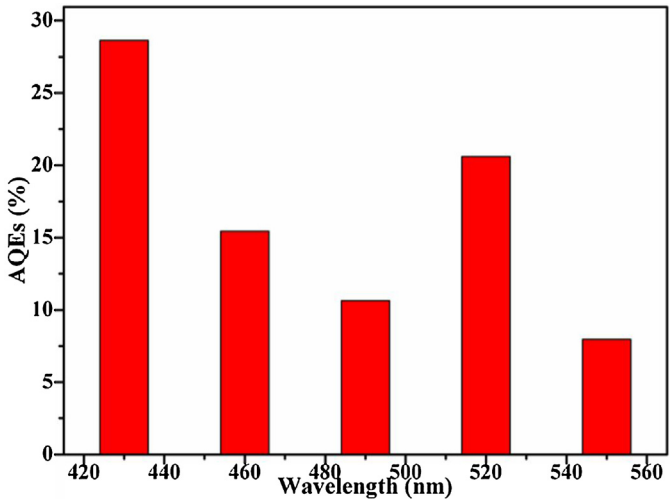


**Fig. 13.** The apparent quantum efficiencies (AQEs) of I-RGO/Ag photocatalyst with EY sensitization under a wide range of visible light irradiation from 400 to 600 nm.

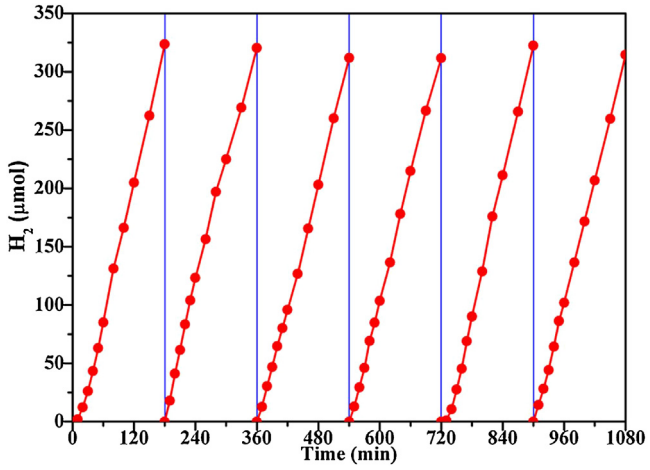


**Fig. 14.** The stability of $H_2$ evolution over I-RGO/Ag photocatalyst under visible light irradiation ($\lambda \geq 420$ nm). The reaction was continued for 1080 min. After every run, the catalysts were collected by centrifuging from the reaction mixture and redistributed in the fresh 10% TEOA aqueous solution with 70 mg EY and then evacuated.

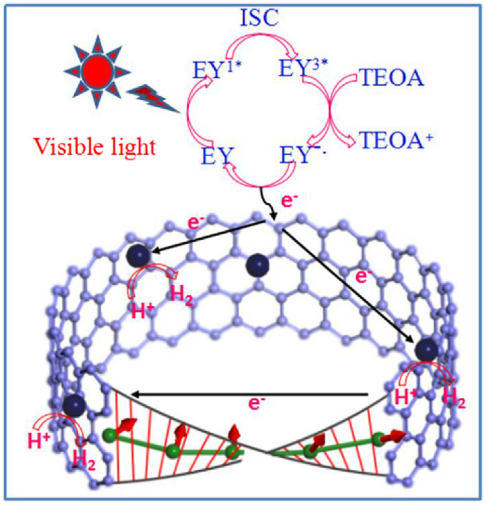


**Scheme 2.** The proposed reaction mechanism for visible-light-driven water splitting by I-RGO/Ag photocatalyst with EY sensitization.

$EY^{3*}$ can be quenched by TEOA to produce $EY^{-\bullet}$ and oxidative donor ($TEOA^+$) [67–73]. The $e^-$ from $EY^{-\bullet}$ specie is transferred to RGO by the noncovalent $\pi$-$\pi$ stacking interaction due to its electron transport characteristics, which leads to spatially separation of photogenerated charges [74–85]. The accumulated electrons on the surface of RGO would transfer along the polyiodides tunneling of Möbius strip-like RGO, which give rise to restrain effectively the anisotropy of the electron and promote the electron rapid transfer on the surface of RGO, leading to the reduce of photogenerated carriers recombination and the prolong of photogenerated electron lifetime. Subsequently, these electrons driven the reduction of $H^+$ to form $H_2$ over Ag NPs.

## 4. Conclusion

In this work, the Möbius strip-like RGO was achieved *via* polyiodides opening an electron tunneling on the surface and between two sides of RGO. The flip-flop electron tunneling takes place *via* strong Rashba spin-orbit coupling between polyiodides and C atoms of RGO by the polyiodides active electrons living in the p orbitals and it can bridge the easier transfer route not only between far-located carbon atoms on the surface of RGO, but also between two sides of RGO through the polyiodides p orbitals. This tunneling gave rise to the electron rapid transfer on the surface and between two sides of RGO, resulting in the conductivity of the Möbius strip-like RGO was remarkably increased and the lifetime of photogenerated charges was largely prolonged. The structure and chemical states of iodine species were characterized through XPS and XRD spectroscopy. The results indicated that I species were in the forms of $I_3^-$ and $I_5^-$ clusters. I–V curves showed the Möbius strip-like RGO exhibited better electrical conductivity and could enhance electron transfer properties, which remarkably reduced the recombination of photogenerated carries, and prolonged the lifetime of photogenerated electron. With the help of these properties, the obtained I-RGO/Ag photocatalyst presented a highly $H_2$ generation activity under visible light irradiation. 318.8 μmol $H_2$ was evolved over I-RGO/Ag photocatalyst in 3 h, about 3.3 time higher than that of un-iodine RGO/Ag. In addition, no remarkable decay of $H_2$ evolution activity was observed in 1080 min reaction. The highest AQE value of 28.8% was achieved at 430 nm.

## Acknowledgment

This work is supported by the NSF of China (grant no. 21433007, 21173242 and 21673262), respectively.

## References

[1] J.R. Farrell, C.A. Mirkin, I.A. Guzei, L.M. Liable-Sands, A.L. Rheingold, Angew. Chem. Int. Ed. 37 (1998) 465–467.
[2] B.J. Holliday, C.A. Mirkin, Angew. Chem. Int. Ed. 40 (2001) 2022–2043.
[3] E.L. Spitler, C.A. Johnson, M.M. Haley, Chem. Rev. 106 (2006) 5344–5386.
[4] N.C. Gianneschi, P.A. Bertin, S.T. Nguyen, C.A. Mirkin, L.N. Zakharov, A.L. Rheingold, J. Am. Chem. Soc. 125 (2003) 10508–10509.
[5] R.P. John, M. Park, D. Moon, K. Lee, S. Hong, Y. Zou, C.S. Hong, M.S. Lah, J. Am. Chem. Soc. 129 (2007) 14142–14143.
[6] N. Zhao, H. Dong, S. Yang, C.P. Sun, Phys. Rev. B 79 (2009) 125440.
[7] D.J. Ballon, H.U. Voss, Phys. Rev. Lett. 101 (2008) 247701.
[8] E.L. Starostin, G.H.M. Van Der Heijden, Nature Mater. 6 (2007) 563–567.
[9] S. Tanda, T. Tsuneta, Y. Okajima, K. Inagaki, K. Yamaya, N. Hatakenaka, Nature (London) 417 (2002) 397–398.
[10] S.C.F. Kui, J.S. Huang, R.W.Y. Sun, N. Zhu, C.M. Che, Angew. Chem. Int. Ed. 45 (2006) 4663–4666.
[11] D. Ajami, O. Oeckler, A. Simon, R. Herges, Nature (London) 426 (2003) 819–821.
[12] Z. Li, Q.S. Wang, C. Kong, Y.Q. Wu, Y.X. Li, G.X. Lu, J. Phys. Chem. C 119 (2015) 13561–13568.
[13] G. Lalwani, J.L. Sundararaj, K. Schaefer, T. Button, B. Sitharaman, J. Mater. Chem. B 2 (2014) 3519–3530.
[14] G.X. Lu, B. Tian, J. Mol. Catal. (China) 31 (2017) 101–104.

[15] R.A. Hoyt, E.M. Remillard, E.D. Cubuk, C.D. Vecitis, E. Kaxiras, J. Phys. Chem. C 121 (2017) 609–615.
[16] D. Jiang, S. Dai, J. Phys. Chem. C 112 (2008) 5348–5351.
[17] Z.L. Guo, Z.R. Gong, H. Dong, C.P. Sun, Phys. Rev. B 80 (2009) 195319.
[18] Z. Li, L.R. Ram-Mohan, Phys. Rev. B 85 (2012) 195438.
[19] C.L. Li, Z.Q. Lei, Q.Z. Wang, F. Cao, F. Wang, W.F. Shangguan, J. Mol. Catal. (China) 29 (2015) 382–389.
[20] L. Li, Y.P. Huang, A.Q. Zhang, M.M. Xiang, J. Yang, M.K. Jia, J. Mol. Catal. (China) 30 (2016) 470–479.
[21] E.T. Cui, G.X. Lu, Int. J. Hydrogen Energy 39 (2014) 8959–8968.
[22] C. Kong, S.X. Min, G.X. Lu, Int. J. Hydrogen Energy 39 (2014) 4836–4844.
[23] X.Q. Hao, Z.L. Jin, H. Yang, G.X. Lu, Y.P. Bi, Appl. Catal. B 210 (2017) 45–56.
[24] W.L. Zhen, H.B. Gao, B. Tian, J.T. Ma, G.X. Lu, ACS Appl. Mater. Interfaces 8 (2016) 10808–10819.
[25] H.D. Li, L. Wang, Z.H. Lan, Y.S. Zheng, Phys. Rev. B 79 (2009) 155429.
[26] M.J. Allen, V.C. Tung, R.B. Kaner, Chem. Rev. 110 (2010) 132–135.
[27] G. Eda, G. Fanchini, M. Chhowalla, Nat. Nanotechnol. 3 (2008) 270–274.
[28] H.L. Wang, J.T. Robinson, X.L. Li, H.J. Dai, J. Am. Chem. Soc. 131 (2009) 9910–9911.
[29] Y.F. Zhan, B.D. Zhang, L.M. Cao, X.X. Wu, Z.P. Lin, X. Yu, X.X. Zhang, D.R. Zeng, F.Y. Xie, W.H. Zhang, J. Chen, H. Meng, Carbon 94 (2015) 1–8.
[30] S.F. Pang, H.K. Yuan, Y.J. Wu, F. Shi, J. Mol. Catal. (China) 31 (2017) 105–120.
[31] D.C. Elias, R.R. Nair, T.M.G. Mohiuddin, S.V. Morozov, P. Blake, M.P. Halsall, A.C. Ferrari, D.W. Boukhvalov, M.I. Katsnelson, A.K. Geim, K.S. Novoselov, Science 323 (2009) 610–613.
[32] Z. Wang, W. Wang, M. Wang, X. Meng, J. Li, J. Mater. Sci. 48 (2013) 2284–2289.
[33] G. Kalita, K. Wakita, M. Takahashi, M. Umeno, J. Mater. Chem. 21 (2011) 15209–15213.
[34] Q. Luo, Y. Zhang, C.Y. Liu, J.B. Li, N. Wang, H. Lin, J. Mater. Chem. 3 (2015) 15996–16004.
[35] N. Jung, N. Kim, S. Jockusch, N.J. Turro, P. Kim, L. Brus, Nano Lett. 9 (2009) 4133–4137.
[36] L. Grigorian, K.A. Williams, S. Fang, G.U. Sumanasekera, A.L. Loper, E.C. Dickey, S.J. Pennycook, P.C. Eklund, Phy. Rev. Lett. 80 (1998) 5560–5563.
[37] T. Michel, L. Alvarez, J.L. Sauvajol, R. Almairac, R. Aznar, O. Mathon, J.L. Bantignies, E. Flahaut, J. Phy. Chem. Solids 67 (2006) 1190–1192.
[38] X.Q. Zhang, G.X. Lu, Carbon 108 (2016) 215–224.
[39] Z. Li, B. Tian, W.Y. Zhang, X.Q. Zhang, Y.Q. Wu, G.X. Lu, Appl. Catal. B 204 (2017) 33–42.
[40] W.Y. Zhang, G.X. Lu, Catal. Sci. Technol. 6 (2016) 7693–7697.
[41] I.Y. Jeon, H.J. Choi, M. Choi, J.M. Seo, S.M. Jung, M.J. Kim, S. Zhang, L.P. Zhang, Z.H. Xia, L.M. Dai, N. Park, J.B. Baek, Sci. Rep. 3 (2013) 1810.
[42] W.S. Hummers, R.E. Offeman, J. Am. Chem. Soc. 80 (1958) 1339.
[43] N.I. Kovtyukhova, P.J. Ollivier, B.R. Martin, T.E. Mallouk, S.A. Chizhik, E.V. Buzaneva, A.D. Gorchinskiy, Chem. Mater. 11 (1999) 771–779.
[44] S. Stankovich, R.D. Piner, X.Q. Chen, N.Q. Wu, S.T. Nguyen, R.S. Ruoff, J. Mater. Chem. 16 (2016) 155–158.
[45] S. Stankovich, D.A. Dikin, R.D. Piner, K.A. Kohlhaas, A. Kleinhammes, Y.Y. Jia, Y. Wu, S.T. Nguyen, R.S. Ruoff, Carbon 45 (2007) 1558–1565.
[46] H.K. Jeong, Y.P. Lee, R.J.W.E. Lahaye, M.H. Park, K.H. An, I.J. Kim, C.W. Yang, C.Y. Park, R.S. Ruoff, Y.H. Lee, J. Am. Chem. Soc. 130 (2008) 1362–1366.
[47] T. Shimidzu, T. Iyoda, Y. Koide, J. Am. Chem. Soc. 107 (1985) 35–41.
[48] Q.Y. Li, L. Chen, G.X. Lu, J. Phys. Chem. C 111 (2007) 11494–11499.
[49] Z. Li, Y.Q. Wu, G.X. Lu, Appl. Catal. B 188 (2016) 56–64.
[50] Z. Li, C. Kong, G.X. Lu, Int. J. Hydrogen Energy 40 (2015) 9061–9068.
[51] Z. Li, B. Tian, W.L. Zhen, Y.Q. Wu, G.X. Lu, Appl. Catal. B 203 (2017) 408–415.
[52] G.X. Lu, S.B. Li, Int. J. Hydrogen Energy 17 (1992) 767–770.
[53] G.X. Lu, H.X. Gao, J.S. Suo, S.B. Li, Chem. Commun. 21 (1994) 2423–2424.
[54] L.P. Wang, G.Y. Wang, J. Mol. Catal. (China) 29 (2015) 275–287.
[55] K. Kalyanasundaram, J. Kiwi, M. Graetzel, Helv. Chim. Acta. 61 (1978) 2720–2730.
[56] Y.Q. Wu, G.X. Lu, S.B. Li, J. Photochem. Photobiol. A 181 (2006) 263–267.
[57] E.T. Cui, G.X. Lu, Int. J. Hydrogen Energy 39 (2014) 7672–7685.
[58] W. Gao, W.Y. Zhang, G.X. Lu, Appl. Catal. B 212 (2017) 23–31.
[59] Z.Y. Ma, X.B. Li, L.J. Deng, G. Fan, J. Mol. Catal. (China) 30 (2016) 575–582.
[60] A. Wojcik, P.V. Kamat, ACS Nano. 4 (2010) 6697–6706.
[61] H.J. Yan, J.H. Yang, G.J. Ma, G.P. Wu, X. Zong, Z.B. Lei, J.Y. Shi, C. Li, J. Catal. 266 (2009) 165–168.
[62] X.F. Ning, J. Li, B.J. Yang, W.L. Zhen, Z. Li, B. Tian, G.X. Lu, Appl. Catal. B 212 (2017) 129–139.
[63] H.B. Gao, W.L. Zhen, J.T. Ma, G.X. Lu, Appl. Catal. B 206 (2017) 353–363.
[64] W.Y. Zhang, S.L. Yang, J. Li, W. Gao, Y.B. Deng, W.P. Dong, C.J. Zhao, G.X. Lu, Appl. Catal. B 206 (2017) 89–103.
[65] W.L. Zhen, J.T. Ma, G.X. Lu, Appl. Catal. B. 190 (2016) 12–25.
[66] A.A. Tonkikh, E.D. Obraztsova, E.A. Obraztsova, A.V. Belkin, A.S. Pozharov, Phys. Status Solidi B 249 (2012) 2454–2459.
[67] K. Maeda, M. Eguchi, S.H.A. Lee, W.J. Youngblood, H. Hata, T.E. Mallouk, J. Phys. Chem. C 113 (2009) 7962–7969.
[68] Z. Li, C. Kong, G.X. Lu, J. Phys. Chem. C 120 (2016) 56–63.
[69] W.J. Jiao, Y.Q. Wu, G.X. Lu, H.W. Jin, RSC Adv. 6 (2016) 29538–29544.
[70] W.Y. Zhang, C. Kong, W. Gao, G.X. Lu, Chem. Commun. 52 (2016) 3038–3041.
[71] C. Kong, Z. Li, G.X. Lu, Int. J. Hydrogen Energy 40 (2015) 9634–9641.
[72] C. Kong, Z. Li, G.X. Lu, Int. J. Hydrogen Energy 40 (2015) 5824–5830.
[73] C. Kong, S.X. Min, G.X. Lu, Chem. Commun. 50 (2014) 9281–9283.
[74] C. Kong, S.X. Min, G.X. Lu, ACS Catal. 4 (2014) 2763–2769.
[75] X.J. Zhang, Z.L. Jin, Y.X. Li, S.B. Li, G.X. Lu, J. Power Source 166 (2007) 74–79.
[76] S.X. Min, G.X. Lu, J. Phys. Chem. C 116 (2012) 25415–25424.
[77] B. Tian, B.J. Yang, J. Li, Z. Li, W.L. Zhen, Y.Q. Wu, G.X. Lu, J. Catal. 350 (2017) 189–196.
[78] B. Tian, W.L. Zhen, H.B. Gao, X.Q. Zhang, Z. Li, G.X. Lu, Appl. Catal. B 203 (2017) 789–797.
[79] S.X. Min, F. Wang, G.X. Lu, Catal. Commun. 80 (2016) 28–32.
[80] B. Tian, Z. Li, W.L. Zhen, G.X. Lu, J. Phys. Chem. C. 120 (2016) 6409–6415.
[82] W.Y. Zhang, C. Kong, G.X. Lu, Chem. Commun. 51 (2015) 10158–10161.
[83] Q.Y. Li, G.X. Lu, J. Mol. Catal. A 266 (2007) 75–79.
[84] Q. Lu, C.L. Li, F. Wang, Q.J. Ren, Z. Ren, J. Mol. Catal. (China) 30 (2016) 557–565.
[85] P. He, Y. Chen, W.F. Fu, J. Mol. Catal. (China) 30 (2016) 269–275.